Small-signal Multi-frequency Model for Grid-connected Inverter System with PWM Effect

Guocheng San, Wenlin Zhang, Ran Luo, Xiaoqiang Guo, *Senior Member, IEEE*, Huanhai Xin, *Member, IEEE*, Elisabetta Tedeschi, *Senior Member, IEEE*, and Mariusz Malinowski, *Fellow, IEEE*

***Abstract*—It is a well known fact that pulse width modulation (PWM) produces sideband effects. Taking this point into account, the accuracy of the grid-connected inverter model can be improved. In this paper, considering the aliasing effect of the PWM sideband components on the closed-loop control, a complete representation for the transfer function of the PWM is obtained. Furthermore, a multi-frequency model of grid-connected inverter system is derived. It is convenient for obtaining a PWM gain for grid-connected inverter system, which is PWM-controlled. In order to have an easy physical expression of the effects caused by the sideband components, an approximation is applied to simplify the PWM gain. The stability analysis is used to prove that PWM gain considering PWM effect is more precise than the conventional one. Experimental results verify the effectiveness of our proposal.**

***Index Terms*—Grid-connected inverter, multi-frequency model, pulse width modulation, stability analysis.**

I. Introduction

THE grid-connected inverter has been widely used [1]–[3], in which model and stability analysis is one of the most important issues [4]–[7]. Typically, the state-space and impedance models are used for stability analysis [8]. Since the state space analysis method is limited by the complexity of the system, it cannot fully represent the characteristics of the high-order system. The impedance analysis method is more widely used in the stability analysis of the grid-connected inverter system. Impedance stability analysis first needs to determine the topology of the system, including the structure of a three-phase inverter and grid-connected filter. Meanwhile, the control system of the inverter plays an important role in system stability and should be considered in the impedance model [9].

To achieve an increasing accuracy, factors such as system parameters, control system delay, and phase-locked loop (PLL) have been progressively included in the impedance model, and the influence of these parameters on the system stability has been deeply analyzed [10]–[12]. Impedance stability analysis equalizes the part of the system containing active devices to the power supply, and the rest is equivalent to the load. The power supply part can be expressed in a Thevenin circuit form or a Norton circuit form, and the load part can be expressed in the form of impedance [8]. The stability of the system can be judged by the impedance ratio of load impedance to power supply impedance under the premise that the power supply and the load are stable [13]. This method focuses on the interaction between the grid-connected inverter and the grid or other connected modules. The current-controlled grid-connected inverter is modeled as an ideal current source and paralleled admittance in [9], so that the inverter is equivalent to the Norton circuit impedance model. As a result, the design and stability analysis of the grid-connected system are simplified. The Norton circuit impedance model and the switching function model of the inverter are compared in [14]. It is pointed out that when the DC voltage disturbance is ignored and the switching frequency is much larger than the frequency studied in the system, the two models are equivalent. The dead zone and switching time of the switch have been considered in the impedance model in [15]. The calculation delay is considered in [16] and an accurate Norton equivalent model is established. It should be noted that the above-mentioned analysis is based on linear sinusoidal PWM modulator, where the sideband components generated by PWM modulator are neglected. In other words, the PWM gain is constant. In practice, however, this is not the case. By using high-order filters, such as an LCL filter, LLCL filter, LTCL filter, etc., the resonance frequency of the filter can be designed to be near or even beyond the Nyquist frequency for a cost-effective design without degrading the quality of the grid-connected current [17]–[19]. In this case, the sideband components may have a significant impact on the dynamics of the inverters. In [20], the multiple-frequency input admittance model of the inverter above the Nyquist frequency is derived. However, it just considers the sideband components generated by the sampling processes, while neglecting the sideband components generated by PWM modulator.

This paper is organized as follows. In Section 2, considering all the sideband components and the aliasing effect, a multi-frequency small signal model of PWM is derived. In Section 3, the multi-frequency small signal model is applied in an inverter system. As a result, the multi-frequency model of LCL-type

Manuscript received November 21, 2019; revised January 15, 2020; accepted February 17, 2020. Date of online publication 6 April, 2020; date of current version March 19, 2020. This work was supported by the National Natural Science Foundation of China (51677161) and Natural Science Foundation of Hebei Province (E2019203563).

G. C. San, W. L. Zhang, R. Luo and X. Guo (corresponding author, e-mail: yeduming@163.com) are with Yanshan University, Qinhuangdao, China.

H. Xin is with Zhejiang University, Hangzhou, China.

E. Tedeschi is with the Department of Electric Power Engineering, Norwegian University of Science and Technology, 7491 Trondheim, Norway.

M. Malinowski is with the Institute of Control and Industrial Electronics, Warsaw University of Technology, 00-662 Warsaw, Poland.

DOI: 10.17775/CSEEJPES.2019.03020

grid-connected inverter system is proposed. Moreover, since the proposed model transfer function is quite complex, an approximate method is used to simplify the loop gain expression and a PWM gain is obtained. To verify the effectiveness of the proposed model, based on impedance analysis, the stability analysis results of a conventional PWM gain and the PWM gain considering PWM effect are compared in Section 4. In addition, the Hardware-In-the-Loop (HIL) test bench is used to verify the proposal. Finally, the conclusion is presented in Section 5.

II. Small-signal Model of PWM

A. Multi-frequency Small Signal Model of PWM

For a grid-connected inverter system, assuming it is a sinusoidal PWM, the fundamental signal of the modulated wave has the following form:

$$V_{\text{mod}}(t) = m_{\text{d}} \sin(\omega_0 t + \theta_0) \tag{1}$$

where m_{d} is the modulation index, ω_0 is the fundamental angular frequency, θ_0 is the fundamental phase. In practical systems, the fundamental signal often consists of two parts, namely the steady-state part V_{mod} and the disturbance (small-signal) part $\hat{v}_{\text{mod}}(t)$. It can be expressed as:

$$v_{\text{mod}}(t) = V_{\text{mod}}(t) + \hat{v}_{\text{mod}}(t) \tag{2}$$

where $\hat{v}_{\text{mod}}(t) = \hat{V}_{\text{mod}} \text{e}^{\text{j}(\omega t+\theta)}$, and ω is an angular frequency of the small-signal disturbance.

When the modulated wave is subjected to bipolar modulation and the frequency of the carrier signal is sufficiently high level, the portion of the modulating signal between the two peaks of the carrier can be considered as a segment based on a linear approximation. As shown in Fig. 1, assuming that any two peak points of the carrier correspond to time points KT_{s} and $(k+1)T_{\text{s}}$, the fundamental wave and the carrier intersect at points $(k+0.5)T_{\text{s}} - 0.5D_{\text{y}}T_{\text{s}}$ and $(k+0.5)T_{\text{s}} + 0.5D_{\text{y}}T_{\text{s}}$, respectively. T_0 represents the distance from the peak point time to the edge of the original duty cycle signal, $T_0 = 0.5(T_{\text{s}} - D_{\text{y}}T_{\text{s}})$. If there is a small disturbance signal, the corresponding disturbance of the duty cycle signal will also appear on both sides of the original duty cycle signal, respectively, as $\hat{d}_{\text{y}}^{-}T_{\text{s}}$ and $\hat{d}_{\text{y}}^{+}T_{\text{s}}$, after linearization, $\hat{d}_{\text{y}}^{-}T_{\text{s}} = \hat{d}_{\text{y}}^{+}T_{\text{s}}$. The duty cycle signal can be expressed as:

$$d_{\text{y}}T_{\text{s}} = D_{\text{y}}T_{\text{s}} + 2\hat{d}_{\text{y}}^{+}T_{\text{s}} = D_{\text{y}}T_{\text{s}} + 2\hat{d}_{\text{y}}^{-}T_{\text{s}} \tag{3}$$

V_{m} is the amplitude of the carrier, and according to the geometric relationship, it is easy to obtain:

$$\frac{\hat{d}_{\text{y}}^{+}T_{\text{s}}}{v_{\text{mod}} - V_{\text{mod}}} = \frac{1}{4}\frac{T_{\text{s}}}{V_{\text{m}}} = \frac{\hat{d}_{\text{y}}^{-}T_{\text{s}}}{v_{\text{mod}} - V_{\text{mod}}} \tag{4}$$

Considering $v_{\text{mod}} - V_{\text{mod}} = \hat{v}_{\text{mod}}$, (4) could be written:

$$\hat{d}_{\text{y}}^{+}T_{\text{s}} = \frac{1}{4}\frac{T_{\text{s}}}{V_{\text{m}}}\hat{v}_{\text{mod}} = \hat{d}_{\text{y}}^{-}T_{\text{s}} \tag{5}$$

According to the area equivalence principle, if $\hat{d}_{\text{y}}^{+}T_{\text{s}}$ and $\hat{d}_{\text{y}}^{-}T_{\text{s}}$ are small enough, they can be approximated as an impulse signal with an impact strength of $(T_{\text{s}}/4\ V_{\text{m}})\hat{v}_{\text{mod}}$. Based on this approximation, the small signal of the kth switching duty cycle can be expressed as the sum of the impulse signals at the time of $kT_{\text{s}} + T_0$ and $(k+1)T_{\text{s}} - T_0$, which is:

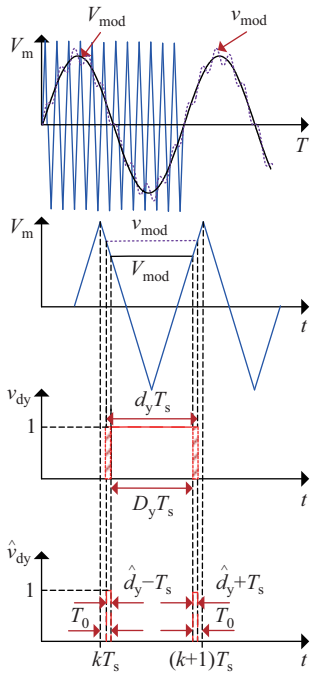

Fig. 1. Schematic diagram of PWM modulation with small-signal disturbance.

$$\hat{d}_{\text{yk}}(t) = \frac{1}{4}\frac{1}{V_{\text{m}}}[\hat{v}_{\text{mod}}(kT_{\text{s}})\delta(t - kT_{\text{s}} - T_0) + \hat{v}_{\text{mod}}((k+1)T_{\text{s}})\delta(t - (k+1)T_{\text{s}} + T_0)] \tag{6}$$

The small signal disturbance in the modulated wave can be expressed as the sum of the impulse signals in an infinite number of switching cycles, so the actual output duty cycle small signal disturbance size can be expressed as:

$$\hat{d}_{\text{y}}(t) = \sum_{k=0}^{\infty}\hat{d}_{\text{yk}}(t) = \frac{1}{4}\frac{1}{V_{\text{m}}}\sum_{k=0}^{\infty}\hat{v}_{\text{mod}}(kT_{\text{s}})[\delta(t - kT_{\text{s}} - T_0) + \delta(t - (k+1)T_{\text{s}} + T_0)] \tag{7}$$

Performing the Laplace transform of (7) gives:

$$\begin{aligned}\hat{d}_{\text{y}}(s) &= \int_{-\infty}^{\infty}\hat{d}_{\text{y}}(t)\text{e}^{-st}\text{d}t \\ &= \int_{-\infty}^{\infty}\frac{1}{4}\frac{1}{V_{\text{m}}}\sum_{k=0}^{\infty}\hat{v}_{\text{mod}}(kT_{\text{s}})[\delta(t - kT_{\text{s}} - T_0) \\ &\quad + \delta(t - (k+1)T_{\text{s}} + T_0)]\text{e}^{-st}\text{d}t\end{aligned} \tag{8}$$

By exchanging the integral and summing order, (8) is equal to:

$$\hat{d}_{\text{y}}(s) = \frac{1}{4}\frac{1}{V_{\text{m}}}\sum_{k=0}^{\infty}\hat{v}_{\text{mod}}(kT_{\text{s}})\left[\int_{-\infty}^{\infty}[\delta(t - kT_{\text{s}} - T_0)\text{e}^{-st} + \delta(t - (k+1)T_{\text{s}} + T_0)\text{e}^{-st}]\text{d}t\right] \tag{9}$$

According to the sampling nature of the impulse function, (9) is simplified as:

$$\hat{d}_{\mathrm{y}}(s)=\frac{1}{4}\frac{1}{V_{\mathrm{m}}}\sum_{k=0}^{\infty}\hat{v}_{\mathrm{mod}}(kT_{\mathrm{s}})\left[\mathrm{e}^{-s(kT_{\mathrm{s}}+T_0)}+\mathrm{e}^{-s((k+1)T_{\mathrm{s}}-T_0)}\right] \tag{10}$$

In (10), $\sum_{k=0}^{\infty}\hat{v}_{\mathrm{mod}}(kT_{\mathrm{s}})\mathrm{e}^{-s(kT_{\mathrm{s}})}$ is the Laplace transform of $\hat{v}_{\mathrm{mod}}(t)$, (10) is rewritten as:

$$\hat{d}_{\mathrm{y}}(s)=\frac{1}{4}\frac{1}{V_{\mathrm{m}}}\left[\mathrm{e}^{-T_0 s}+\mathrm{e}^{-(T_{\mathrm{s}}-T_0)s}\right]\hat{v}_{\mathrm{mod}}(s) \tag{11}$$

Therefore, the transfer function from $\hat{v}_{\mathrm{mod}}(s)$ to $\hat{d}_{\mathrm{y}}(s)$ is:

$$\frac{\hat{d}_{\mathrm{y}}(s)}{\hat{v}_{\mathrm{mod}}(s)}=\frac{1}{4}\frac{1}{V_{\mathrm{m}}}\left[\mathrm{e}^{-T_0 s}+\mathrm{e}^{-(T_{\mathrm{s}}-T_0)s}\right] \tag{12}$$

And because $T_0 = 0.5\ (T_{\mathrm{s}} - D_{\mathrm{y}}T_{\mathrm{s}})$, it can be obtained:

$$\frac{\hat{d}_{\mathrm{y}}(s)}{\hat{v}_{\mathrm{mod}}(s)}=\frac{1}{4}\frac{1}{V_{\mathrm{m}}}\mathrm{e}^{-\frac{1}{2}T_{\mathrm{s}}s}(\mathrm{e}^{+\frac{1}{2}D_{\mathrm{y}}T_{\mathrm{s}}s}+\mathrm{e}^{-\frac{1}{2}D_{\mathrm{y}}T_{\mathrm{s}}s}) \tag{13}$$

From the Euler's formula and $s = \mathrm{j}\omega$, the small-signal model in the frequency domain is obtained:

$$\frac{\hat{d}_{\mathrm{y}}(\mathrm{j}\omega)}{\hat{v}_{\mathrm{mod}}(\mathrm{j}\omega)}=\frac{1}{2}\frac{1}{V_{\mathrm{m}}}\cos\left(\frac{1}{2}\omega D_{\mathrm{y}}T_{\mathrm{s}}\right)\mathrm{e}^{-\mathrm{j}\frac{1}{2}\omega T_{\mathrm{s}}} \tag{14}$$

In fact, PWM is a typical nonlinear sampling section, and there are many other frequency components in addition to the fundamental frequency. When the fundamental frequency of the small signal disturbance is ω, the duty cycle signal obtained through the sampling section contains not only the fundamental frequency component of ω, but also the sideband components at frequencies $\omega + n\omega_{\mathrm{s}}$ ($n = 0, \pm 1, \pm 2\ldots$), where ω_{s} is the sampling angular frequency. This characteristic of the PWM sampling section will cause aliasing effects in the loop of the closed-loop operation of the system. Especially when the bandwidth of the converter is relatively high, the sideband components cannot be greatly attenuated after passing through the loop, and the aliasing effect is particularly significant. Therefore, the impact of the sideband components must be considered when modeling the PWM to improve the accuracy of the modeling.

According to (12) and (13), it can be noted:

$$\begin{aligned}\frac{\hat{d}_{\mathrm{y}}(s)}{\hat{v}_{\mathrm{mod}}(s)}&=G_{\mathrm{m}}=G_{\mathrm{m}}^{-}+G_{\mathrm{m}}^{+}\\ G_{\mathrm{m}}^{-}&=\frac{1}{4}\frac{1}{V_{\mathrm{m}}}\mathrm{e}^{-\frac{1}{2}T_{\mathrm{s}}s}\mathrm{e}^{+\frac{1}{2}D_{\mathrm{y}}T_{\mathrm{s}}s}\\ G_{\mathrm{m}}^{+}&=\frac{1}{4}\frac{1}{V_{\mathrm{m}}}\mathrm{e}^{-\frac{1}{2}T_{\mathrm{s}}s}\mathrm{e}^{-\frac{1}{2}D_{\mathrm{y}}T_{\mathrm{s}}s}\end{aligned} \tag{15}$$

According to the equal area criterion, $\hat{d}_{\mathrm{y}}$ can be approximated as a superposition of a series of pulse function areas, and in the kth period, the area of $\hat{d}_{\mathrm{yk}}(t)$ is $\hat{d}_{\mathrm{yk}}T_{\mathrm{s}}$, so that:

$$\begin{aligned}\hat{v}_{\mathrm{dy}}(t)=\sum_{k=-\infty}^{\infty}\hat{d}_{\mathrm{yk}}T_{\mathrm{s}}\Bigg[&\delta\left(t-\left(k+\frac{1}{2}\right)T_{\mathrm{s}}+\frac{1}{2}D_{\mathrm{y}}T_{\mathrm{s}}\right)\\&+\delta\left(t-\left(k+\frac{1}{2}\right)T_{\mathrm{s}}-\frac{1}{2}D_{\mathrm{y}}T_{\mathrm{s}}\right)\Bigg]\end{aligned} \tag{16}$$

Substituting (15) into (16) yields:

$$\begin{aligned}\hat{v}_{\mathrm{dy}}(t)=\hat{v}_{\mathrm{mod}}T_{\mathrm{s}}\sum_{k=-\infty}^{\infty}\Bigg[&G_{\mathrm{m}}^{-}\delta\left(t-\left(k+\frac{1}{2}\right)T_{\mathrm{s}}+\frac{1}{2}D_{\mathrm{y}}T_{\mathrm{s}}\right)\\&+G_{\mathrm{m}}^{+}\delta\left(t-\left(k+\frac{1}{2}\right)T_{\mathrm{s}}-\frac{1}{2}D_{\mathrm{y}}T_{\mathrm{s}}\right)\Bigg]\end{aligned} \tag{17}$$

According to the Fourier series definition and the Fourier coefficient F_{n} shown in (18), the Fourier transform of (17) can be obtained:

$$f(t)=\sum_{n=-\infty}^{\infty}F_{\mathrm{n}}\mathrm{e}^{-\mathrm{j}\omega t},F_{\mathrm{n}}=\frac{1}{T}\int_{-\frac{T}{2}}^{\frac{T}{2}}f(t)\mathrm{e}^{-\mathrm{j}n\omega t}\mathrm{d}t \tag{18}$$

$$\begin{aligned}\hat{v}_{\mathrm{dy}}(t)=&G_{\mathrm{m}}^{-}\hat{v}_{\mathrm{mod}}T_{\mathrm{s}}\sum_{n=-\infty}^{\infty}F_{\mathrm{n}}\mathrm{e}^{-\mathrm{j}n\omega_{\mathrm{s}}t}\\&+G_{\mathrm{m}}^{+}\hat{v}_{\mathrm{mod}}T_{\mathrm{s}}\sum_{n=-\infty}^{\infty}F_{\mathrm{n}}\mathrm{e}^{-\mathrm{j}n\omega_{\mathrm{s}}t}\end{aligned} \tag{19}$$

where F_{n} is the Fourier coefficient of the $n\omega_{\mathrm{s}}$ component. If only the range of the interval [0, T_{s}] and the impulse function is considered, the detailed expression is:

$$\begin{aligned}F_{\mathrm{n}}&=\frac{1}{T_{\mathrm{s}}}\int_{-\frac{T_{\mathrm{s}}}{2}}^{\frac{T_{\mathrm{s}}}{2}}\sum_{n=-\infty}^{\infty}\Bigg[\delta\left(t-\frac{1}{2}T_{\mathrm{s}}+\frac{1}{2}D_{\mathrm{y}}T_{\mathrm{s}}\right)\\&\quad+\delta\left(t-\frac{1}{2}T_{\mathrm{s}}-\frac{1}{2}D_{\mathrm{y}}T_{\mathrm{s}}\right)\Bigg]\mathrm{e}^{-\mathrm{j}n\omega_{\mathrm{s}}t}\mathrm{d}t\\&=\frac{1}{T_{\mathrm{s}}}\left[\mathrm{e}^{-\mathrm{j}\pi n(1-D_{\mathrm{y}})}+\mathrm{e}^{-\mathrm{j}\pi n(1+D_{\mathrm{y}})}\right]\end{aligned} \tag{20}$$

Substituting (2) and (20) into (19) yields:

$$\begin{aligned}\hat{v}_{\mathrm{dy}}(t)=\sum_{\mathrm{n}=-\infty}^{\infty}V_{\mathrm{mod}}\Bigg[&G_{\mathrm{m}}^{-}\mathrm{e}^{\mathrm{j}(\omega+n\omega_{\mathrm{s}})t-\mathrm{j}\pi n(1-D_{\mathrm{y}})+\theta}\\&+G_{\mathrm{m}}^{+}\mathrm{e}^{\mathrm{j}(\omega+n\omega_{\mathrm{s}})t-\mathrm{j}\pi n(1+D_{\mathrm{y}})+\theta}\Bigg]\end{aligned} \tag{21}$$

According to (21), it can be clearly seen that after the Fourier series analysis, the sinusoidal disturbance signal $\hat{v}_{\mathrm{mod}}(t)$ of frequency ω causes a change in the duty cycle signal. $\hat{v}_{\mathrm{dy}}(t)$ has sideband components of the frequency $\omega + n\omega_{\mathrm{s}}$ ($n = 0, \pm 1, \pm 2\ldots$). Taking the frequency $\omega + n\omega_{\mathrm{s}}$ as a whole to analysis:

$$\begin{aligned}\hat{v}_{\mathrm{dy\_n}}(t)=\hat{v}_{\mathrm{mod}}(t)\Bigg[&G_{\mathrm{m}}^{-}\mathrm{e}^{\mathrm{j}n\omega_{\mathrm{s}}t-\mathrm{j}\pi n(1-D_{\mathrm{y}})}\\&+G_{\mathrm{m}}^{+}\mathrm{e}^{\mathrm{j}n\omega_{\mathrm{s}}t-\mathrm{j}\pi n(1+D_{\mathrm{y}})}\Bigg]\end{aligned} \tag{22}$$

For $\hat{v}_{\mathrm{mod}}(t)$ and $\hat{v}_{\mathrm{dy\_n}}(t)$ to write their Fourier coefficients at ω and $\omega + n\omega_{\mathrm{s}}$ as $\hat{v}_{\mathrm{mod}}(\mathrm{j}\omega)$ and $\hat{v}_{\mathrm{dy}}[\mathrm{j}(\omega+n\omega_{\mathrm{s}})]$, respectively. They are:

$$\begin{aligned}\hat{v}_{\mathrm{mod}}(\mathrm{j}\omega)&=V_{\mathrm{mod}}\mathrm{e}^{\mathrm{j}\theta}\\ \hat{v}_{\mathrm{dy}}[\mathrm{j}(\omega+n\omega_{\mathrm{s}})]&=V_{\mathrm{mod}}\Bigg[G_{\mathrm{m}}^{-}\mathrm{e}^{-\mathrm{j}\pi n(1-D_{\mathrm{y}})+\theta}\\&\quad+G_{\mathrm{m}}^{+}\mathrm{e}^{-\mathrm{j}\pi n(1+D_{\mathrm{y}})+\theta}\Bigg]\end{aligned} \tag{23}$$

According to (23), there is:

$$\frac{\hat{v}_{\mathrm{dy}}[\mathrm{j}(\omega+n\omega_{\mathrm{s}})]}{\hat{v}_{\mathrm{mod}}(\mathrm{j}\omega)}=\left[G_{\mathrm{m}}^{-}\mathrm{e}^{-\mathrm{j}\pi n(1-D_{\mathrm{y}})}+G_{\mathrm{m}}^{+}\mathrm{e}^{-\mathrm{j}\pi n(1+D_{\mathrm{y}})}\right] \tag{24}$$

Analyzing (24), the response of the two parts in $\hat{v}_{\mathrm{dy}}[\mathrm{j}(\omega+n\omega_{\mathrm{s}})]$ is different. Although the values are different in magnitude and phase, the properties are the same, so it can be analyzed on either side. Analyzing, for example, the second addend on the right hand side, the amplitude of $\hat{v}_{\mathrm{dy}}[\mathrm{j}(\omega+n\omega_{\mathrm{s}})]^{+}$ is always G_{m}^{+}, regardless of the size of n. In phase, it will be delayed by $\pi n\ (1+D_{\mathrm{y}})$ compared to $\hat{v}_{\mathrm{dy}}[\mathrm{j}\omega]^{+}$, which is related to the size of n. In summary, the resulting multi-frequency small signal model of PWM can be clearly represented by Fig. 2.

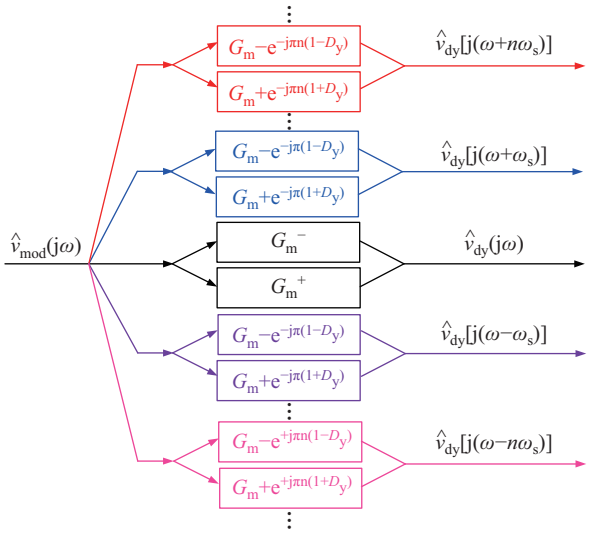

Fig. 2. Multi-frequency small signal model of PWM.

B. Aliasing Effect of PWM

In the actual grid-connected inverter system, $\hat{v}_{\mathrm{dy}}(t)$ contains the component of the small signal disturbance frequency and the sideband components it causes. In turn, the output voltage of the inverter side is affected, and the output voltage of the inverter side affects the current of the grid connected inverter. Therefore, the disturbance small signal frequency and the sideband components are included in the grid-connected current. Finally, in the current closed-loop control, all frequency components are repeatedly fed back in the PWM section, causing the disturbance frequency component and the sideband components to also be included in $\hat{v}_{\mathrm{mod}}$. If all sideband components are considered, the spectral width of $\hat{v}_{\mathrm{mod}}$ is much higher than the Nyquist frequency $\omega_{\mathrm{s}}/2$.

According to the Nyquist sampling theorem, after $\hat{v}_{\mathrm{mod}}$ passes through the PWM section, the duty cycle spectrum generated by the high-frequency component ($>\omega_{\mathrm{s}}/2$) and the low-frequency component ($<\omega_{\mathrm{s}}/2$) in $\hat{v}_{\mathrm{mod}}$ will overlap. This is the aliasing effect of the PWM section [21]. Based on (24), The transfer function of each frequency component $\omega+m\omega_{\mathrm{s}}(m=0,\pm1,\pm2\ldots)$ in the modulated wave with each frequency component of the duty cycle signal is:

$$\frac{\hat{v}_{\mathrm{dy}}[\mathrm{j}(\omega+n\omega_{\mathrm{s}})]}{\hat{v}_{\mathrm{mod}}[\mathrm{j}(\omega+m\omega_{\mathrm{s}})]}=\left[G_{\mathrm{m}}^{-}\mathrm{e}^{-\mathrm{j}\pi(n-m)(1-D_{\mathrm{y}})}+G_{\mathrm{m}}^{+}\mathrm{e}^{-\mathrm{j}\pi(n-m)(1+D_{\mathrm{y}})}\right] \tag{25}$$

(25) can be directly expressed as:

$$\begin{aligned}&\hat{v}_{\mathrm{dy}}[\mathrm{j}(\omega+n\omega_{\mathrm{s}})]\\&=G_{\mathrm{m}}^{-}\mathrm{e}^{-\mathrm{j}\pi n(1-D_{\mathrm{y}})}\sum_{m=-\infty}^{\infty}[\mathrm{j}(\omega+m\omega_{\mathrm{s}})]\mathrm{e}^{\mathrm{j}\pi m(1-D_{y})}\\&\quad+G_{\mathrm{m}}^{+}\mathrm{e}^{-\mathrm{j}\pi n(1+D_{\mathrm{y}})}\sum_{m=-\infty}^{\infty}[\mathrm{j}(\omega+m\omega_{\mathrm{s}})]\mathrm{e}^{\mathrm{j}\pi m(1+D_{y})}\end{aligned} \tag{26}$$

In special cases, when $n=0$, there are:

$$\begin{aligned}\hat{v}_{\mathrm{dy}}[\mathrm{j}\omega]=&G_{\mathrm{m}}^{-}\sum_{m=-\infty}^{\infty}[\mathrm{j}(\omega+m\omega_{\mathrm{s}})]\mathrm{e}^{\mathrm{j}\pi m(1-D_{y})}\\&G_{\mathrm{m}}^{+}\sum_{m=-\infty}^{\infty}[\mathrm{j}(\omega+m\omega_{\mathrm{s}})]\mathrm{e}^{\mathrm{j}\pi m(1+D_{y})}\end{aligned} \tag{27}$$

According to (27), when $n=0$, $\hat{v}_{\mathrm{dy}}[\mathrm{j}\omega]$ can be represented by the block diagram of Fig. 3. Comparing (26) and (27), $\hat{v}_{\mathrm{dy}}[\mathrm{j}(\omega+n\omega_{\mathrm{s}})]$ has the same magnitude as $\hat{v}_{\mathrm{dy}}[\mathrm{j}\omega]$, however, there are initial phase lags of $\pi n\ (1-D_{\mathrm{y}})$ and $\pi n\ (1+D_{\mathrm{y}})$ in the parts of G_{m}^{-} and G_{m}^{+}, respectively.

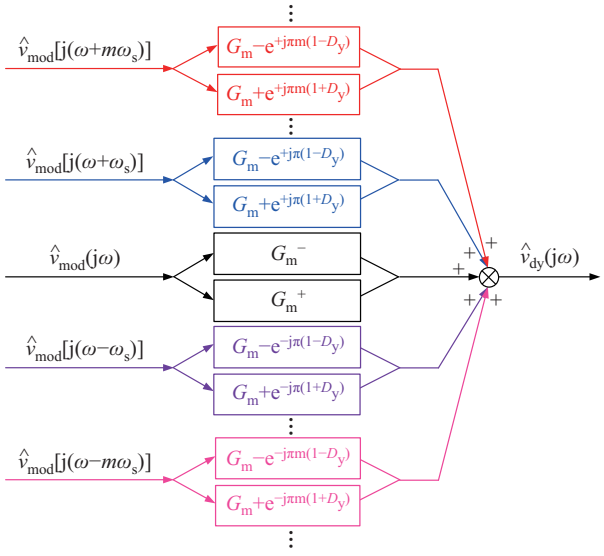

Fig. 3. Multi-frequency feedback PWM small-signal model when $n=0$.

According to Figs. 2–3 and (27), the schematic diagram of the PWM can be obtained in Fig. 4. It provides the aliasing of all sideband frequency components throughout the PWM section.

III. Inverter System Considering the PWM Small-Signal Model

A. Model of Inverter System with Conventional PWM Gain

The block diagram of system control is shown in Figs. 5 and 6, respectively. The physical meaning of each system symbol is shown in Table I. K_{PWM} is a constant which represents the

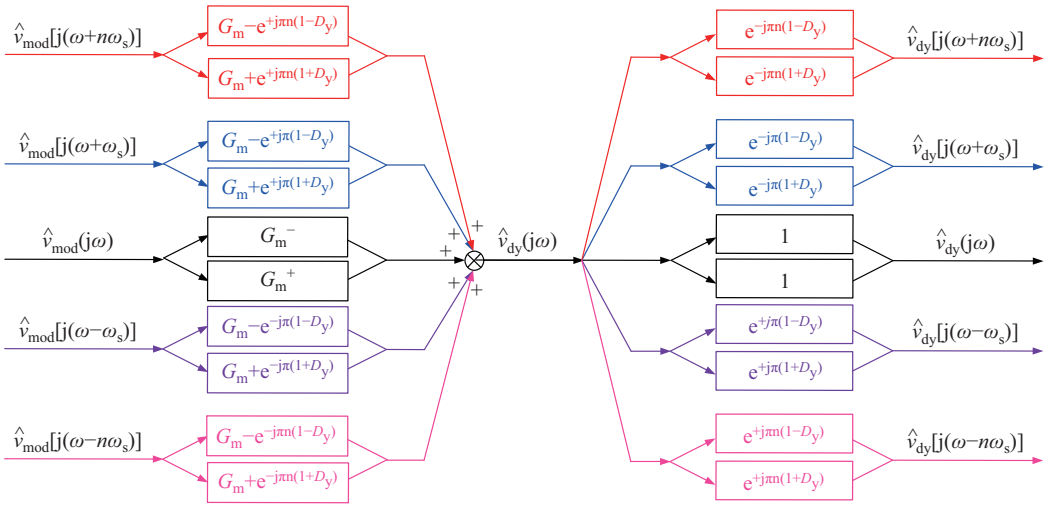

Fig. 4. PWM small signal model considering aliasing effect.

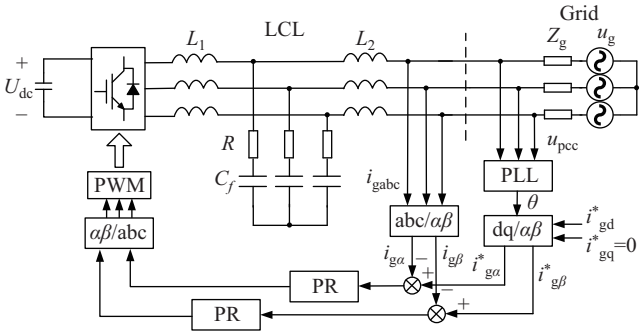

Fig. 5. Scheme of three-phase two-level voltage source grid-connected inverter with LCL filter.

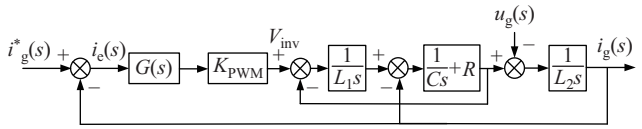

Fig. 6. The block diagram of system control.

traditional PWM section gain. In addition, G (s) is the current controller, and the proportional-resonant (PR) controller is used. According to [8], the Norton equivalent circuit model of the system is shown in Fig. 7.

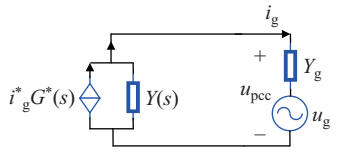

Fig. 7. The Norton equivalent circuit model of the grid-connected inverter system.

B. Model of Grid-connected Inverter System with a PWM Gain Considering PWM Effect

The PWM small-signal model of Fig. 4 is considered in the three-phase grid-connected inverter system. By combining it with the control block diagram of Fig. 6, the control block diagram of the LCL-type grid-connected inverter multi-frequency small-signal model can be obtained, as shown in Fig. 8, where Y^* is the ratio of the grid-connected current to the inverter output voltage, and its value is:

$$Y^*(\mathrm{s}) = \frac{i_\mathrm{g}(\mathrm{s})}{V_\mathrm{inv}(\mathrm{s})} = \frac{RC_f s + 1}{L_1 L_2 C_f s^3 + (L_1 s + L_2 s)(1 + RC_f s)}. \tag{28}$$

The blue dashed box shows the small signal model of PWM shown in Fig. 8, and the green dashed box indicates the K_{PWM} gain including the PWM small signal model, which is denoted as K^*_{PWM}. It is worth mentioning that at the node $\hat{v}_{\mathrm{dy}}(\mathrm{j}\omega)$, each frequency component part is an independent loop.

The expression shown in Fig. 8 is:

$$\begin{aligned} K^*_{\mathrm{PWM}} &= K_{\mathrm{PWM}} G_{\mathrm{PWM}}(\mathrm{j}\omega) = K_{\mathrm{PWM}} \frac{\hat{v}_{\mathrm{dy}}(\mathrm{j}\omega)}{\hat{v}_{\mathrm{mod}}(\mathrm{j}\omega)} \\ &= \frac{K_{\mathrm{PWM}}(G^-_\mathrm{m} + G^+_\mathrm{m})}{1 + \sum\limits_{\substack{n=-\infty \\ n\neq 0}}^{+\infty} (G^-_\mathrm{m} + G^+_\mathrm{m}) H[\mathrm{j}(\omega + n\omega_\mathrm{s})]} \end{aligned} \tag{29}$$

where $H\ [\mathrm{j}(\omega + n\omega_\mathrm{s})] = G\ [\mathrm{j}(\omega + n\omega_\mathrm{s})]\ K_{\mathrm{PWM}} Y^*\ [\mathrm{j}(\omega + n\omega_\mathrm{s})]$, represents the loop gain of the sideband components of $\omega + n\omega_\mathrm{s}$. According to (29), the size of K^*_{PWM} is related to $H[\mathrm{j}(\omega + n\omega_\mathrm{s})]$, so K^*_{PWM} is not fixed. According to (29), Fig. 8 can be simplified to obtain a simple control block diagram of the LCL-type grid-connected inverter multi-frequency model as shown in Fig. 9. In addition, the gain of the entire complete control loop is:

$$H_{\mathrm{com}}(\mathrm{j}\omega) = \frac{H(\mathrm{j}\omega)}{1 + \sum\limits_{\substack{n=-\infty \\ n\neq 0}}^{+\infty} (G^-_\mathrm{m} + G^+_\mathrm{m}) H[\mathrm{j}(\omega + n\omega_\mathrm{s})]}. \tag{30}$$

The transfer function of the PR controller can be expressed as:

$$G(s) = k_\mathrm{p} + \frac{k_\mathrm{r} s}{s^2 + \omega_0^2} \tag{31}$$

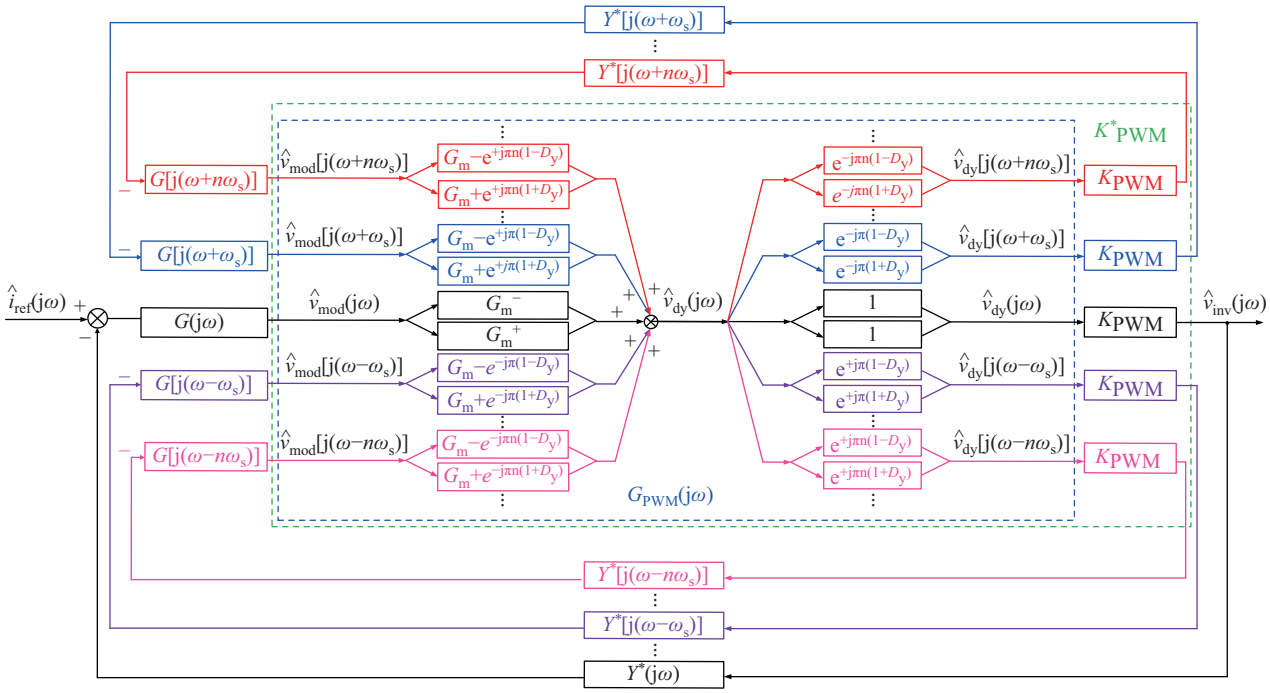

Fig. 8. Control block diagram of multi-frequency model about three-phase two-level voltage source grid-connected inverter with LCL filter.

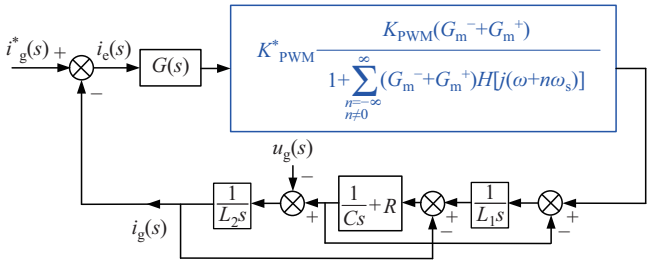

Fig. 9. Simple control block diagram of the multi-frequency model.

where k_p is the proportional coefficient and k_r is the resonance coefficient. The PR controller's corner frequency is much smaller than the system's cutoff frequency, so analyzing the sideband frequency, the gain of the PR controller can be approximated as a single proportional gain. There is:

$$G[j(\omega + n\omega_s)] = k_p \tag{32}$$

Then, (29) can be written as:

$$K^*_{PWM} = \frac{K_{PWM} \times (G_m^- + G_m^+)}{1 + \sum\limits_{\substack{n=-\infty \\ n\neq 0}}^{+\infty} (G_m^- + G_m^+) k_p K_{PWM} Y^*[j(\omega + n\omega_s)]} \tag{33}$$

In (33), the amount of infinity can be expressed as [21], [22]:

$$\sum_{\substack{n=-\infty \\ n\neq 0}}^{+\infty} (G_m^- + G_m^+) k_p K_{PWM} Y^*[j(\omega + n\omega_s)]$$

$$\approx (G_m^- + G_m^+) k_p K_{PWM} \left(\sum_{\substack{n=-\infty \\ n\neq 0}}^{+\infty} Y^*[j(\omega + n\omega_s)] - Y^*(j\omega) \right)$$

$$\approx (G_m^- + G_m^+) k_p K_{PWM} T_s \left[Y^{**}(j\omega) - \frac{1}{T_s} Y^*(j\omega) \right] \tag{34}$$

where $Y^{**}(j\omega)$ is a function expression after sampling $Y^*(j\omega)$, and the sampling period is T_s. $Y^*(s)$ has been given in the previous description, so there is:

$$Y^*(j\omega) = \frac{(j\omega)RC_f + 1}{(j\omega)^3 L_1 L_2 C_f + (j\omega)^2 (L_1 + L_2) RC_f + (j\omega)(L_1 + L_2)} \tag{35}$$

$$Y^{**}(j\omega) = \frac{1}{(L_1 + L_2)} \frac{1}{e^{j\omega T_s} - 1} - \frac{1}{(L_1 + L_2)} \frac{1}{(A - B)} \left(\frac{A}{e^{(j\omega + 0.5A)T_s} - 1} + \frac{B}{e^{(j\omega + 0.5B)T_s} - 1} \right) \tag{36}$$

where,

$$A = \frac{(L_1 + L_2)R}{L_1 L_2} + \sqrt{\left(\frac{(L_1 + L_2)R}{L_1 L_2} \right)^2 - \frac{4(L_1 + L_2)}{L_1 L_2 C_f}}$$

$$B = \frac{(L_1 + L_2)R}{L_1 L_2} - \sqrt{\left(\frac{(L_1 + L_2)R}{L_1 L_2} \right)^2 - \frac{4(L_1 + L_2)}{L_1 L_2 C_f}} \tag{37}$$

Although the result of (36) is very accurate, due to the existence of $e^{(j\omega+0.5A)Ts}$ and $e^{(j\omega+0.5B)Ts}$, the result of (37) is difficult to relate to the physical meaning of the model. It is assumed that $AT_s \ll 1$, $BT_s \ll 1$. Therefore, the Pade approximation is used to simplify some factors in (37). They

are:

$$e^{j\omega T_s} \approx \frac{1+0.5(j\omega)T_s+[\frac{(j\omega)T_s}{\pi}]^2}{1-0.5(j\omega)T_s+\left[\frac{(j\omega)T_s}{\pi}\right]^2} \tag{38}$$

$$e^{(j\omega+0.5A)T_s} \approx \frac{1+0.5(j\omega+0.5A)T_s+[\frac{(j\omega+0.5A)T_s}{\pi}]^2}{1-0.5(j\omega+0.5A)T_s+\left[\frac{(j\omega+0.5A)T_s}{\pi}\right]^2}$$

$$e^{(j\omega+0.5B)T_s} \approx \frac{1+0.5(j\omega+0.5B)T_s+[\frac{(j\omega+0.5B)T_s}{\pi}]^2}{1-0.5(j\omega+0.5B)T_s+\left[\frac{(j\omega+0.5B)T_s}{\pi}\right]^2}$$

Substituting (37) and (38) into (36), there is:

$$Y^{**}(j\omega) = \frac{1}{T_s}Y^*(j\omega) - \frac{T_s R}{\pi^2 L_1 L_2} \tag{39}$$

Substituting (39) into (34) yields:

$$\sum_{\substack{n=-\infty \\ n\neq 0}}^{+\infty} (G_m^- + G_m^+)k_p K_{PWM} Y^*[j(\omega+n\omega_s)]$$
$$\approx -\frac{(G_m^- + G_m^+)k_p K_{PWM} T_s^2 R}{\pi^2 L_1 L_2} \tag{40}$$

Substituting (40) into (33) yields a simplified new PWM gain K^*_{PWM}:

$$K^*_{PWM} \approx \frac{K_{PWM} \times (G_m^- + G_m^+)}{1-\frac{(G_m^- + G_m^+)k_p K_{PWM} T_s^2 R}{\pi^2 L_1 L_2}}. \tag{41}$$

Above all, the new impendence model can be obtained. It is worth noting that K^*_{PWM} should indicate the relationship between modulation wave and output voltage of the inverter, and the magnitude of the G_m represents pulse width of the duty cycle signal. Hence, the magnitude of the G_m should be ignored at this time. In other words, the disturbance of the pulse width can be regarded as a dead zone, which will not affect the stability analysis.

IV. Stability Analysis and Experimental Verification

A. Stability Analysis

The stability of the system is judged by the Nyquist curve of the equivalent impedance ratio between the grid and the inverter. If the characteristic curve of the impedance ratio (i.e., $Z_g(s)/Z(s)$) does not encircle the point $(-1, j0)$, the system is stable. Otherwise, the system is unstable [8], [9].

Based on (41), K_{PWM} and K^*_{PWM} have been compared through a bode diagram. Fig. 10 shows a comparison of K_{PWM}/K^*_{PWM} when the switching frequency is 20 kHz, 10 kHz and 5 kHz, respectively. Since the Pade approximation is used in the simplification of the loop gain expression and the assumption $AT_s \ll 1$, $BT_s \ll 1$ is made, the applicability of K^*_{PWM}, that is, the minimum switching frequency range, is still worthy of further study. This paper chooses the switching frequency of 20 kHz.

After the inverter system selected in this paper is designed, the parameters are shown in Table I. The results of stability analyses with different PWM gains are the main research

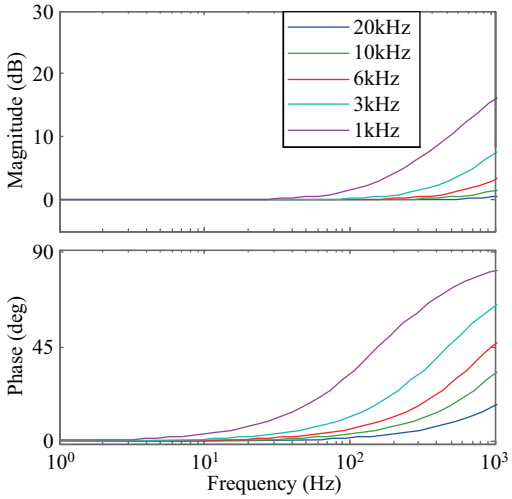

Fig. 10. Bode plot of K_{PWM}/K^*_{PWM}.

TABLE I
PARAMETERS OF GRID-CONNECTED INVERTER SYSTEM

Parameter	System symbol	value
DC bus voltage	U_{dc}	1000 V
Grid voltage	u_g	220 V(RMS)
PCC voltage	u_{PCC}	—
Rated current	I_g^*	30 A
Grid-connected current	i_g	—
Switching frequency	f_{sw}	20 kHz
Filter inductor 1	L_1	3.8 mH
Filter inductor 2	L_2	1.3 mH
Filter capacitor	C_f	12.7 μF
Grid impedance	$Z_g(R_g + L_g)$	0.1 Ω/—
Series passive damping	R	12 Ω
Current controller	$K_p/K_r/\omega_0$	0.15/20/100 π

object. Therefore, the bandwidth of the PLL is set low enough, and the dynamics of PLL on system stability is ignored [23]. At the same time, the sampling frequency set in this paper is the same as the frequency of the PWM, considering a certain calculation delay and highlighting the role of the PWM small signal model [24], [25]. Based on the above analysis, the Nyquist curve with K_{PWM} and K^*_{PWM} in different Z_g is shown in Fig. 11. According to the position of the point $(-1, j0)$ (red "+" in Fig. 11), it can be clearly seen that when L_g is between 6.5 mH and 8.5 mH, the outcome of the system stability assessment is different depending on the use of K_{PWM} or K^*_{PWM}. As a result, a more detailed comparison is shown in Fig. 12.

Figure 12(a) shows that the Nyquist curves of both K_{PWM} and K^*_{PWM} do not encircle the point $(-1, j0)$ when L_g is 6.5 mH, the system at this time is considered stable regardless of the PWM gain. However, it can be clearly seen in Fig. 12(b) that the Nyquist curve of K_{PWM} encircles the point $(-1, j0)$, but the Nyquist curve of K^*_{PWM} does not encircle the point $(-1, j0)$ when L_g is 7.5 mH. In other words, there is a difference in the assessment of system stability when using different PWM gains. The Nyquist curve of K_{PWM} indicates that the system is unstable, on the contrary, the Nyquist curve of K^*_{PWM} indicates that the system is stable. In addition, as can be seen from Fig. 12(c), Nyquist curves of both K_{PWM} and K^*_{PWM} encircle the point $(-1, j0)$ when L_g is 8.5 mH,

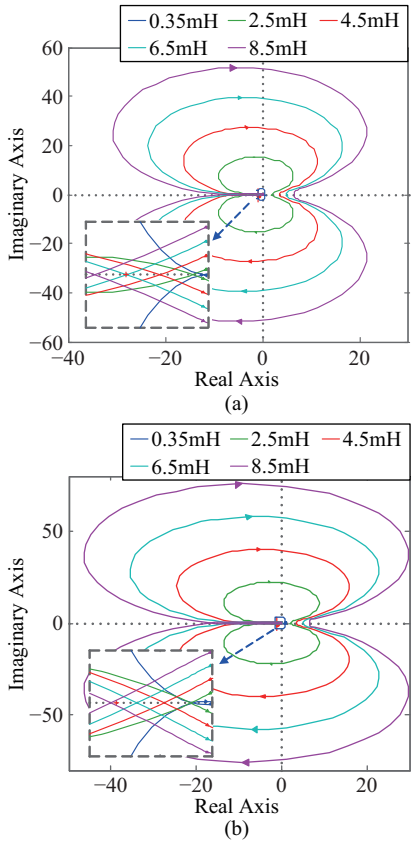

Fig. 11. The Nyquist curve of $Z_g(s)/Z(s)$ with K_{PWM} (a) and K^*_{PWM} (b).

the system at this time is considered unstable. The reason for the difference in the case $L_g = 7.5$ mH, is that K^*_{PWM} is more precise than K_{PWM}, which will be confirmed in the next Section.

B. Experimental Verification

Hardware-In-the-Loop (HIL) platform is useful for development and validation of converters [26]–[28]. Therefore, it is used in this paper. Fig. 13 illustrates the system schematic and control block diagram. The controller is designed with a 20 kHz PWM carrier frequency, for which a HIL with 0.5 μs sampling time and a 0.5 μs latency is an excellent match. For the inverter system, the HIL sampling time needs to be faster. A good rule of the thumb is that the HIL sampling frequency needs to be higher than the carrier frequency [29].

The hardware and setup are shown in Fig. 14. Then, Figs. 15–17 gives experimental results to verify the stability of the system and these results are obtained through a DA output and oscilloscope. As shown in these figures, the full-load grid-connected current is set to 30A, and the half-load is set to 15A. The stability of the system is proved not only by the steady-state waveforms at full-load and half-load but also by the dynamic response of full-load to half-load and half-load to full-load. It can be clearly seen from Fig. 15 and Fig. 16 that when L_g is 6.5 mH and 7.5 mH, the PCC voltage and grid-connected current are normal, and when i^*_g is changed, the steady-state can be restored in a short time, i.e. the dynamic response is rapid. Fig. 17 shows that when L_g is 8.5 mH, the PCC voltage and grid-connected current are

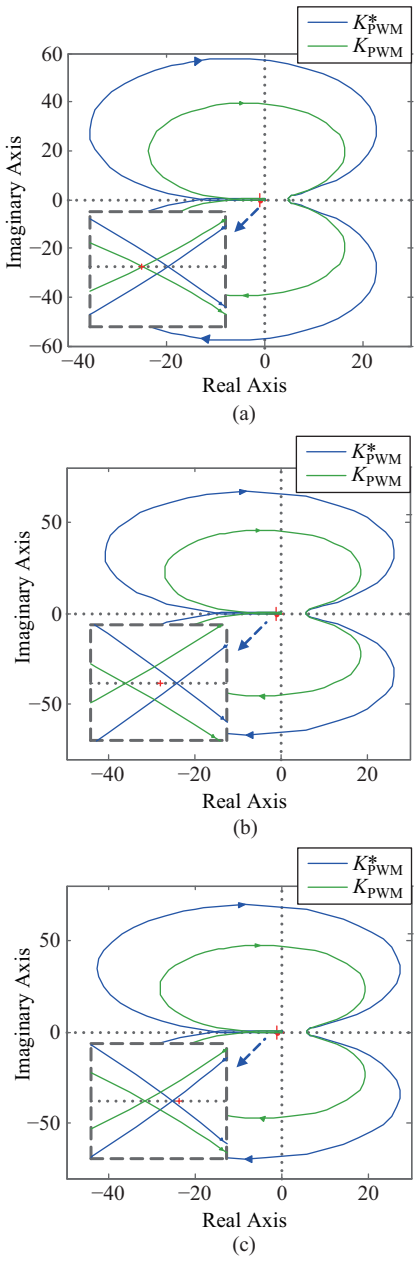

Fig. 12. Comparison of the Nyquist curve with K_{PWM} and K^*_{PWM} under (a) $L_g = 6.5$ mH, (b) $L_g = 7.5$ mH and (c) $L_g = 8.5$ mH.

highly distorted, meanwhile, when i^*_g is changed, almost no change has occurred.

Experimental results of dynamically switching L_g are shown in Figs. 18–20. At the rising edge of the purple signal, L_g switches from 0 mH to 6.5 mH, 7.5 mH and 8.5 mH, respectively. And at the falling edge, L_g switches back to 0 mH. It can be clearly seen that when L_g switches from 0 mH to 6.5 mH and 7.5 mH, the PCC voltage and grid-connected currents have small fluctuations but can return to normal, and the grid-connected current and PCC voltage can maintain the same phase. However, when L_g switches from 0 mH to 8.5 mH, both the grid-connected current and PCC voltage are seriously distorted, and when L_g switches back to 0 mH, the system still cannot run normally. Based on the above analysis, the system is stable when L_g is 6.5 mH and

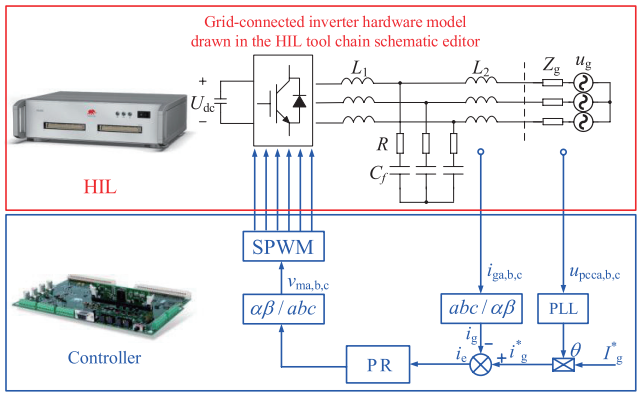

Fig. 13. The schematic of the grid-connected inverter (upper frame) modeled in the HIL device, and the controller (lower frame) under test.

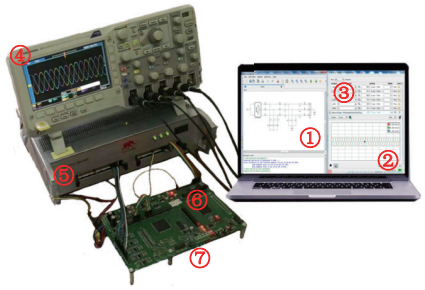

Fig. 14. HIL environment: ①, ②, ③–HIL toolchain, ④–Oscilloscope, ⑤–HIL Typhoon 602, ⑥–Controller, ⑦–DA output.

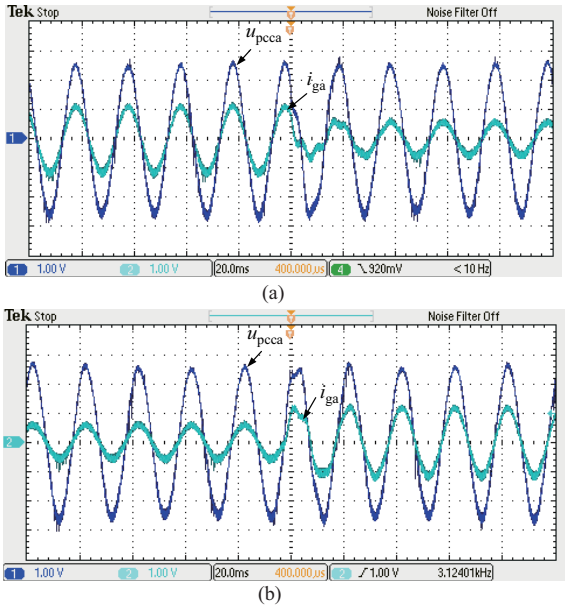

(a)

(b)

Fig. 15. Dynamic experimental results of grid-connected voltage and grid-connected current when $L_g = 6.5$ mH: (a) full-load to half-load (b) half-load to full-load.

7.5 mH, and the system is considered to be unstable when L_g is 8.5 mH. This is consistent with the stability analysis with K^*_{PWM}, while the stability analysis with K_{PWM} is inaccurate when L_g is 7.5 mH. The experimental results prove that K^*_{PWM} is more precise than K_{PWM}.

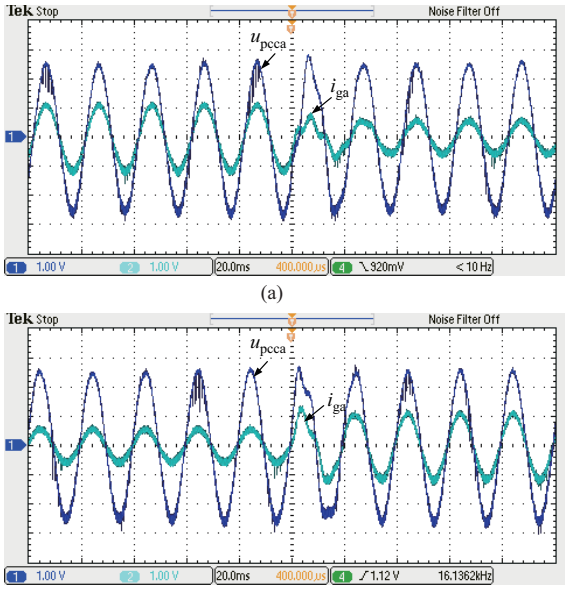

(a)

(b)

Fig. 16. Dynamic experimental results of grid-connected voltage and grid-connected current when $L_g = 7.5$ mH: (a) full-load to half-load (b) half-load to full-load.

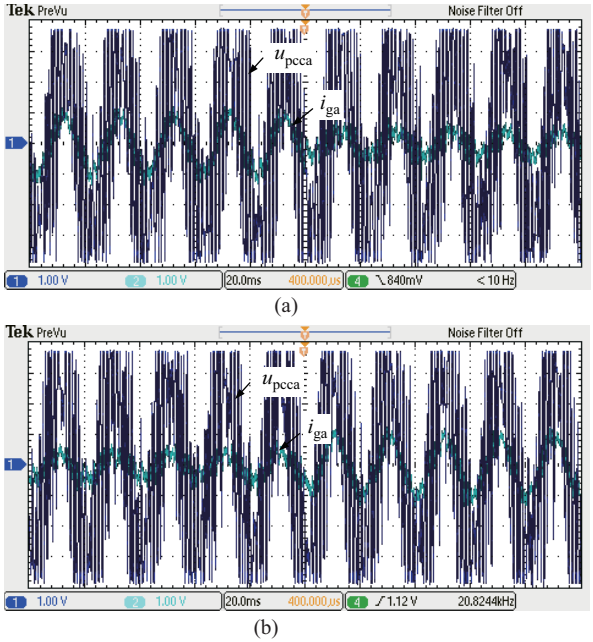

(a)

(b)

Fig. 17. Dynamic experimental results of grid-connected voltage and grid-connected current when $L_g = 8.5$ mH: (a) full-load to half-load (b) half-load to full-load.

V. Conclusion

When sideband components and aliasing effects of PWM are considered in the modeling of grid-connected inverter system, a small-signal model with multi-frequency range can be obtained. This model provides precise modulator gain expressions and loop gain expressions, and provides accurate stability information under practical conditions. The precise expressions are difficult to use in a practical grid-connected inverter system. Appropriate simplification yields an approximate expression, which provides a convenient and more intuitive interpretation of the sideband components. Moreover,

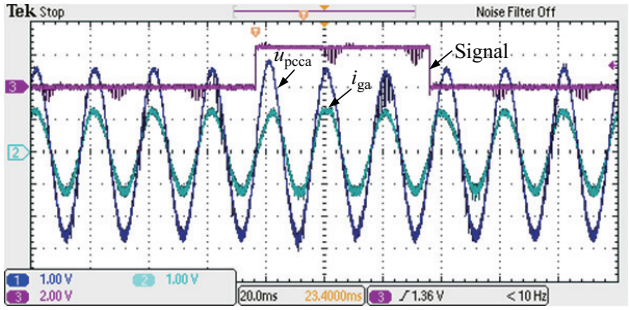

Fig. 18. Dynamic experimental results of switching L_g when $L_g = 6.5$ mH.

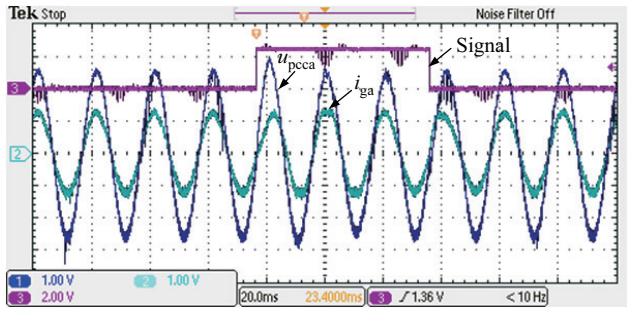

Fig. 19. Dynamic experimental results of switching L_g when $L_g = 7.5$ mH.

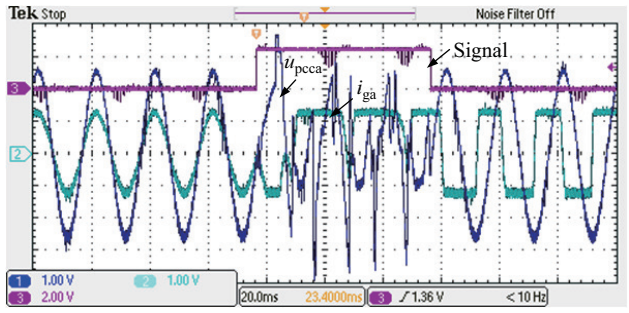

Fig. 20. Dynamic experimental results of switching L_g when $L_g = 8.5$ mH.

based on the multi-frequency model, a PWM gain K^*_{PWM} has been obtained. By using the impedance analysis method, the influence of the grid-side inductance L_g on the system stability is analyzed. The experimental results show that when L_g is 7.5 mH, the system is stable, which is consistent with the theoretical analysis of K^*_{PWM}, and is contrary to the theoretical analysis of K_{PWM}. Meanwhile, the experimental results when L_g is 6.5 mH and 7.5 mH are also consistent with the theoretical analysis. Therefore, this proves that K^*_{PWM} is more accurate than the conventional K_{PWM} in stability analysis around the influence of grid-side inductance L_g. In addition, the HIL platform and associated software is used for rapid development and experimental verification of the grid-connected inverter system with obvious availability and high flexibility. The next study will focus on the measurement of specific sideband components and the design or stability analysis of other systems.

REFERENCES

[1] H. Wu and X. F. Wang, "Design-oriented transient stability analysis of grid-connected converters with power synchronization control," *IEEE Transactions on Industrial Electronics*, vol. 66, no. 8, pp. 6473–6482, Aug. 2019.

[2] M. F. Firuzi, A. Roosta, and M. Gitizadeh, "Stability analysis and decentralized control of inverter-based AC microgrid," *Protection and Control of Modern Power Systems*, vol. 4, no. 1, pp. 6, Mar. 2019.

[3] B. Li, J. W. He, Y. Li, and B. T. Li, "A review of the protection for the multi-terminal VSC-HVDC grid," *Protection and Control of Modern Power Systems*, vol. 4, no. 1, pp. 21, Nov. 2019.

[4] X. F. Wang, F. Blaabjerg, and W. M. Wu, "Modeling and analysis of harmonic stability in an AC power-electronics-based power system," *IEEE Transactions on Power Electronics*, vol. 29, no. 12, pp. 6421–6432, Dec. 2014.

[5] V. Miranda, "Successful large-scale renewables integration in Portugal: Technology and intelligent tools," *CSEE Journal of Power and Energy Systems*, vol. 3, no. 1, pp. 7–16, Mar. 2017.

[6] F. R. Badal, P. Das, S. K. Sarker, and S. K. Das, "A survey on control issues in renewable energy integration and microgrid," *Protection and Control of Modern Power Systems*, vol. 4, no. 1, pp. 8, Apr. 2019.

[7] J. X. Wang, J. D. Wei, Y. C. Zhu, and X. L. Wang, "The reliability and operation test system of power grid with large-scale renewable integration," *CSEE Journal of Power and Energy Systems*, doi: 10.17775/CSEE-JPES.2017.01300.

[8] J. Sun, "Impedance-based stability criterion for grid-connected inverters," *IEEE Transactions on Power Electronics*, vol. 26, no. 11, pp. 3075–3078, Nov. 2011.

[9] M. Cespedes and J. Sun, "Impedance modeling and analysis of grid-connected voltage-source converters," *IEEE Transactions on Power Electronics*, vol. 29, no. 3, pp. 1254–1261, Mar. 2014.

[10] X. Zhao, L. C. Chang, R. M. Shao, and K. Spence, "Power system support functions provided by smart inverters—A review," *CPSS Transactions on Power Electronics and Applications*, vol. 3, no. 1, pp. 25–35, Mar. 2018.

[11] S. Golestan, J. M. Guerrero, A. Vidal, A. G. Yepes, J. Doval-Gandoy, and F. D. Freijedo, "Small-signal modeling, stability analysis and design optimization of single-phase delay-based PLLs," *IEEE Transactions on Power Electronics*, vol. 31, no. 5, pp. 3517–3527, May 2016.

[12] X. Q. He, H. Geng, and S. K. Ma, "Transient stability analysis of grid-tied converters considering PLL's nonlinearity," *CPSS Transactions on Power Electronics and Applications*, vol. 4, no. 1, pp. 40–49, Mar. 2019.

[13] L. Zhang, Y. T. Zou, J. C. Yu, J. C. Qin, V. Vittal, G. G. Karady, D. Shi, and Z. W. Wang, "Modeling, control, and protection of modular multilevel converter-based multi-terminal HVDC systems: A review," *CSEE Journal of Power and Energy Systems*, vol. 3, no. 4, pp. 340–352, Dec. 2017.

[14] Y. C. Wang, X. Chen, Y. Zhang, J. Chen, and C. Y. Gong, "Impedance modeling of three-phase grid-connected inverters and analysis of interaction stability in grid-connected system," in *Proceedings of the 2016 IEEE 8th International Power Electronics and Motion Control Conference*, Hefei, 2016, pp. 3606–3612.

[15] R. D. Middlebrook and S. Cuk, "A general unified approach to modelling switching-converter power stages," in *Proceedings of 1976 IEEE Power Electronics Specialists Conference*, Cleveland, OH, 1976, pp. 18–34.

[16] X. F. Wang, F. Blaabjerg, M. Liserre, Z. Chen, J. W. He, and Y. W. Li, "An active damper for stabilizing power-electronics-based AC systems," *IEEE Transactions on Power Electronics*, vol. 29, no. 7, pp. 3318–3329, Jul. 2014.

[17] Y. Tang, W. L. Yao, P. C. Loh, and F. Blaabjerg, "Design of LCL filters with LCL resonance frequencies beyond the nyquist frequency for grid-connected converters," *IEEE Journal of Emerging and Selected Topics in Power Electronics*, vol. 4, no. 1, pp. 3–14, Mar. 2016.

[18] Y. Q. Wei, Q. M. Luo, and A. Mantooth, "Comprehensive analysis and design of LLC resonant converter with magnetic control," *CPSS Transactions on Power Electronics and Applications*, vol. 4, no. 4, pp. 265–275, Dec. 2019.

[19] J. B. Xu, J. Yang, J. Ye, Z. X. Zhang, and A. W. Shen, "An LTCL filter for three-phase grid-connected converters," *IEEE Transactions on Power Electronics*, vol. 29, no. 8, pp. 4322–4338, Aug. 2014.

[20] L. Harnefors, R. Finger, X. F. Wang, H. F. Bai, and F. Blaabjerg, "VSC input-admittance modeling and analysis above the nyquist frequency for passivity-based stability assessment," *IEEE Transactions on Industrial Electronics*, vol. 64, no. 8, pp. 6362–6370, Aug. 2017.

[21] X. Li, X. B. Ruan, Q. Jin, M. K. Sha, and C. K. Tse, "Small-signal models with extended frequency range for DC–DC converters with large modulation ripple amplitude," *IEEE Transactions on Power Electronics*, vol. 33, no. 9, pp. 8151–8163, Sep. 2018.

[22] A. V. Oppenheim and R. W. Schafer, *Discrete-Time Signal Processing*, 3rd ed., London, UK: Pearson, 2009.

[23] B. Wen, D. Dong, D. Boroyevich, R. Burgos, P. Mattavelli, and Z. Y. Shen, "Impedance-based analysis of grid-synchronization stability for three-phase paralleled converters," *IEEE Transactions on Power Electronics*, vol. 31, no. 1, pp. 26–38, Jan. 2016.
[24] J. G. Wang, J. D. Yan, L. Jiang, and J. Y. Zou, "Delay-dependent stability of single-loop controlled grid-connected inverters with LCL filters," *IEEE Transactions on Power Electronics*, vol. 31, no. 1, pp. 743–757, Jan. 2016.
[25] J. P. Ma, X. F. Wang, F. Blaabjerg, L. Harnefors, and W. S. Song, "Accuracy analysis of the zero-order hold model for digital pulse width modulation," *IEEE Transactions on Power Electronics*, vol. 33, no. 12, pp. 10826–10834, Dec. 2018.
[26] Y. Liu, Z. P. Xi, Z. G. Liang, W. C. Song, S. Bhattacharya, A. Huang, J. Langston, M. Steurer, W. Litzenberger, L. Anderson, R. Adapa, and A. Sundaram, "Controller hardware-in-the-loop validation for a 10 MVA ETO-based STATCOM for wind farm application," in *Proceedings of 2009 IEEE Energy Conversion Congress and Exposition*, San Jose, CA, 2009, pp. 1398–1403.
[27] D. Westermann and M. Kratz, "A real-time development platform for the next generation of power system control functions," *IEEE Transactions on Industrial Electronics*, vol. 57, no. 4, pp. 1159–1166, Apr. 2010.
[28] C. X. Mao, F. Leng, J. L. Li, S. T. Zhang, L. D. Zhang, R. Mo, D. Wang, J. Zeng, X. Chen, R. R. An, and Y. J. Zhao, "A 400-V/50-kVA digital–physical hybrid real-time simulation platform for power systems," *IEEE Transactions on Industrial Electronics*, vol. 65, no. 5, pp. 3666–3676, May 2018.
[29] E. Adzic, S. Grabic, M. Vekic, V. Porobic, and N. F. Celanovic, "Hardware-in-the-Loop optimization of the 3-phase grid connected converter controller," in *Proceedings of the 39th Annual Conference of the IEEE Industrial Electronics Society*, Vienna, 2013, pp. 5392–5397.

Guocheng San received the M.S. and Ph.D. degrees in Electrical Engineering from Yanshan University, Qinhuangdao, China, in 2007 and 2017. Since 2017, he has been an Associate Professor with the Department of Electrical Engineering, Yanshan University. His current research interests include renewable energy conversion systems.

Wenlin Zhang received the B.S. degree in Electrical Engineering from Hebei University, Baoding, China, in 2017. He is currently pursuing the M.S. degree in Electrical Engineering at Yanshan University, Qinhuangdao, China. His current research interests include the control of grid-connected converters.

Ran Luo received the B.S. degree in Electrical Engineering from Langfang Normal University, Langfang, China, in 2018. She is currently pursuing the M.S. degree in Electrical Engineering at Yanshan University, Qinhuangdao, China. Her current research interests include the control of grid-connected converters.

Xiaoqiang Guo received the B.S. and Ph.D. degrees in Electrical Engineering from Yanshan University, Qinhuangdao, China, in 2003 and 2009, respectively. He has been a Postdoctoral Fellow with the Laboratory for Electrical Drive Applications and Research (LEDAR), Ryerson University, Toronto, ON, Canada. He is currently a professor with the Department of Electrical Engineering, Yanshan University, China. He has authored/coauthored more than eighty technical papers, in addition to eleven patents. His current research interests include high-power converters and AC drives, electric vehicle charging stations, and renewable energy power conversion systems. Dr. Guo is a Senior Member of the IEEE Power Electronics Society and IEEE Industrial Electronics Society. He is currently an Associate Editor of the CPSS Transactions on Power Electronics and Applications, Journal of Power Electronics, and IET Power Electronics.

Huanhai Xin received the Ph.D. degree from the College of Electrical Engineering, Zhejiang University, Hangzhou, China, in 2007. He was a Post-Doctoral Fellow with the Electrical Engineering and Computer Science Department, University of Central Florida, Orlando, Florida from 2009 to 2010. He is currently a Professor with the Department of Electrical Engineering, Zhejiang University. His research interests include distributed control in active distribution grids and microgrids, AC/DC power system transient stability analysis and control, and grid-integration of large-scale renewable energy to weak grids.

Elisabetta Tedeschi received the M.Sc. degree (Hons.) in Electrical Engineering and the Ph.D. degree in Industrial Engineering from the University of Padova, Italy, in 2005 and 2009, respectively. From 2009 to 2011, she was a Postdoc Researcher with the Norwegian University of Science and Technology (NTNU), working on the design and control of energy conversion systems for the grid integration of offshore renewable energies. From 2011 to 2013, she was a Researcher with Tecnalia, Spain, where she was a Principal Investigator in the FP7-Sea2grid Project, related to the storage needs for the grid integration of wave energy converters. She also received a Marie Curie Fellowship. From 2013 to 2014, she was a Research Scientist with SINTEF Energy and an Adjunct Associate Professor with NTNU. In 2014, she became a Full Professor within the offshore grid at NTNU.S.e has led and/or contributed to more than 15 national and international scientific projects and she is the author or co-author of 1 book chapter and more than 15 journals and 50 conference papers in the field of marine energy and energy conversion systems. She has a core competency in the design and control of energy conversion and transmission systems, with a focus on offshore energy, and power-quality issues.

Mariusz Malinowski received the Ph.D. and D.Sc. degrees in Electrical Engineering from the Institute of Control and Industrial Electronics, Warsaw University of Technology (WUT), Warsaw, Poland, in 2001 and 2012, respectively. He was a Visiting Scholar with Aalborg University, Aalborg, Denmark, University of Nevada, Reno, NV, USA, Technical University of Berlin, Berlin, Germany, and ETH Zurich, Zurich, Switzerland. He is currently with the Institute of Control and Industrial Electronics, WUT. He has coauthored over 150 technical papers and six books. His current research interests include the control and the modulation of grid-side converters, multilevel converters, smart grids, and power-generation systems based on renewable energies. Dr. Malinowski was a recipient of the Siemens Prize, in 2002 and 2007, the WUT President Scientic Prize, in 2015, the Polish Minister of Science and the Higher Education Awards, in 2003 and 2008, the Prime Minister of Poland Award for Habilitation, in 2013, the IEEE Industrial Electronics Society (IES) David Irwin Early Career Award, in 2011, and the Bimal Bose Energy Systems Award, in 2015. His industry application received several awards and medals.